Responsibility of small defects for the low radiation tolerance of coated conductors

Responsibility of small defects for the low radiation tolerance of coated conductors

OPEN ACCESS
IOP Publishing
Superconductor Science and Technology
Supercond. Sci. Technol. **37** (2024) 105008 (20pp)
https://doi.org/10.1088/1361-6668/ad70db

Responsibility of small defects for the low radiation tolerance of coated conductors

Raphael Unterrainer[1,*], Davide Gambino[2], Florian Semper[1], Alexander Bodenseher[1], Daniele Torsello[3,4], Francesco Laviano[3,4], David X Fischer[5] and Michael Eisterer[1]

[1] Atominstitut, Technische Universität Wien, 1020 Vienna, Austria
[2] IFM, Linköping University, SE-581 83 Linköping, Sweden
[3] Department of Applied Science and Technology, Politecnico di Torino, I-10129 Torino, Italy
[4] Istituto Nazionale di Fisica Nucleare, Sezione di Torino, I-10125 Torino, Italy
[5] PSFC, Massachusetts Institute of Technology, Cambridge, MA 02139, United States of America

E-mail: raphael.unterrainer@tuwien.ac.at

Received 2 April 2024, revised 30 July 2024
Accepted for publication 19 August 2024
Published 2 September 2024

Abstract

Rare-earth-barium-copper-oxide based coated conductors exhibit a relatively low radiation robustness compared to e.g. Nb_3Sn due to the *d*-wave symmetry of the order parameter, rendering impurity scattering pair breaking. The type and size of the introduced defects influence the degrading effects on the superconducting properties; thus the disorder cannot be quantified by the number of displaced atoms alone. In order to develop degradation mitigation strategies for radiation intense environments, it is relevant to distinguish between detrimental and beneficial defect structures. Gadolinium-barium-copper-oxide based samples irradiated with the full TRIGA Mark II fission reactor spectrum accumulate a high density of point-like defects and small clusters due to n - γ capture reactions of gadolinium. This leads to a 14–15 times stronger degradation of the critical temperature compared to samples shielded from slow neutrons. At the same time both irradiation techniques lead to the same degradation behavior of the critical current density as function of the transition temperature $J_c(T_c)$. Furthermore, annealing the degraded samples displayed the same T_c recovery rates, indicating the universality of the defects responsible for the degradation. Since the primary knock on atom of the n - γ reaction as well as the recoil energy is known, we used molecular dynamics simulations to calculate which defects are formed in the neutron capture process and density functional theory to assess their influence on the local density of states. The defects found in the simulation were mainly single defects as well as clusters consisting of Oxygen Frenkel pairs, however, more complex defects such as Gd^{Cu} antisites occurred as well.

Keywords: coated conductors, neutron irradiation, fusion magnets, molecular dynamics simulations, defect structures, rare-earth-barium-copper-oxide, radiation tolerance

* Author to whom any correspondence should be addressed.

1. Introduction

Advances in conductor technology and an influx of venture capital have ushered a second golden age in nuclear fusion research, exemplified by an ever-growing number of startups, spin-offs and consortia aiming to prove the commercial feasibility of magnetic confinement fusion power plants within this decade [1, 2]. This ambitious goal requires the design of fusion reactors, which need to be affordable to build and maintain in order to ensure their economic viability.

This requirement is translated by modern designs into a decrease of the overall volume with respect to earlier designs like International-Thermonuclear-Experimental-Reactor (ITER) and DEMO (DEMOnstration reactor). To reduce the size while preserving a high production of fusion power, these proposed compact fusion plants rely on stronger magnets, currently only achievable by using coated conductors (CCs) based on rare-earth-barium-copper-oxide (REBCO). This is due to their characteristic high upper critical field B_{c2} and superior critical current density J_c at high fields, that is required for the construction of high field magnets (>20 T) leading to better confinement and higher fusion power density ($P_{\text{Fusion}} \propto B^4$) in comparison to using conventional superconductors such as Nb_3Sn and NbTi.

However, the advantages of small reactor designs come at a price. A recent study evaluating the radiation damage in REBCO expected from the neutron flux and spectrum of ARC (achievable-robust-compact) class reactors [3], indicates that the lifetime of its REBCO based magnet system would be as short as a few months under full power operating conditions. The calculations showed that within 10 years of operation, the introduced defect density would reach values as high as 0.52 dpa (displacement per atom) in the superconducting coils [4]. This value vastly exceeds the reported data for neutron irradiated samples which were exposed to a cumulative fast neutron fluence of $3.3 \times 10^{22}\,\text{m}^{-2}$ corresponding to ∼3–15 mdpa [5], which already leads to a degradation of the critical current at 15 T and 30 K below its pristine values [6].

Although the simulations by Torsello *et al* used an early prototype model of ARC, which can still be optimized in regards of shielding and size, the necessary improvement of 2 orders of magnitude in terms of cumulative damage on the REBCO coils might likely not be achievable without severely increasing the diameter of the reactor. Simulations carried out by Ledda *et al* [7] predict that 50 cm of ZrH_2 shielding would be necessary in order to reduce the expected damage at the toroidal field (TF) coils in 10 full power years to 3 mdpa. In fact, such a neutron shield would increases the TF size, making it more expensive and also difficult to reach the required field in the plasma. Another mitigation strategy would be to anneal the magnets in-situ [8], however the recoverable damage is limited at reasonable temperatures. Though the situation is more promising, understanding precisely the radiation hardness and damage processes of high temperature superconductors becomes even more crucial in order to find the optimal balance between achievable radiation robustness, reactor size and mitigation strategies like annealing.

While, as depicted in figure 1(a), the critical temperature (T_c) of REBCO based commercial CCs was shown to monotonously degrade upon irradiation, the critical current density ($J_c(B > 0)$) initially increases due to improved pinning, before starting to degrade. The fast neutron fluence at which J_c degrades below its pristine value was shown to be dependant on temperature, field and the initial defect density in the samples [6, 9–12]. The behavior of a variety of samples at 30 K and 15 T is visualized in figure 1(b).

Impurity scattering in d-wave superconductors, such as REBCO, is most likely the main reason for their low radiation resistance [13]. Extensive studies have been conducted on evaluating the defect structure and density of large cascades caused by fast neutron ($E > 0.1$ MeV) irradiation [14, 15]. It was found that their mean diameter of approximately 2.5 nm fits well the coherence length of yttrium-barium-copper-oxide (YBCO) ($YBa_2Cu_3O_{7-x}$) $\xi(T = 0) \sim 1.4$ nm, that explains the increase in pinning force. The low reported density of $1 \times 10^{19} - 5 \times 10^{22}\,\text{m}^{-3}$ per 10^{22} fast neutrons/m^2 of these defects, however, does not explain the observed degradation of J_c after its initial increase. Linden *et al* estimated the contribution of the large collision cascades to a reduction of the overall superconducting cross section to be in the region of only 0.01% [14], thus the degradation of the critical current was attributed to small defects [16] not directly visible in conventional scanning transmission electron microscopy images. Statistical analysis of high angle annular dark field lattice images showed an increase of the lattice parameter in heavily He^+ irradiated samples, which is consistent with this assumption [5, 17].

In order to examine the effect of point-like defects on the superconducting properties of REBCO, CCs containing gadolinium-barium-copper-oxide (GdBCO) ($GdBa_2Cu_3O_{7-x}$) were irradiated with the full neutron spectrum of the TRIGA Mark II (Training, Research, Isotopes, General Atomic) reactor of TU Wien instead of shielding them from slow neutrons with cadmium. The high flux of thermal neutrons ($E < 0.5$ eV) leads to the formation of a high density of point-like defects [18]. This is enabled by the high absorption cross section of gadolinium for thermal neutrons. Since the energies of this reaction are well known, we use molecular dynamics (MD) simulations based on a recently developed interatomic potential [19] to analyze the typology and distribution of lattice defects formed in the recoil process together with their formation probabilities. We employ these configurations as an input for density functional theory (DFT) calculations to obtain the effect of such small defects on the electronic density of states (DOS) at the Fermi level, which gives hints about the degradation process of the superconducting properties.

2. Methods

2.1. Neutron irradiation

In previous neutron irradiation experiments performed at TU Vienna, CCs were usually shielded with cadmium foil during irradiation to screen low energy neutrons. This was done to

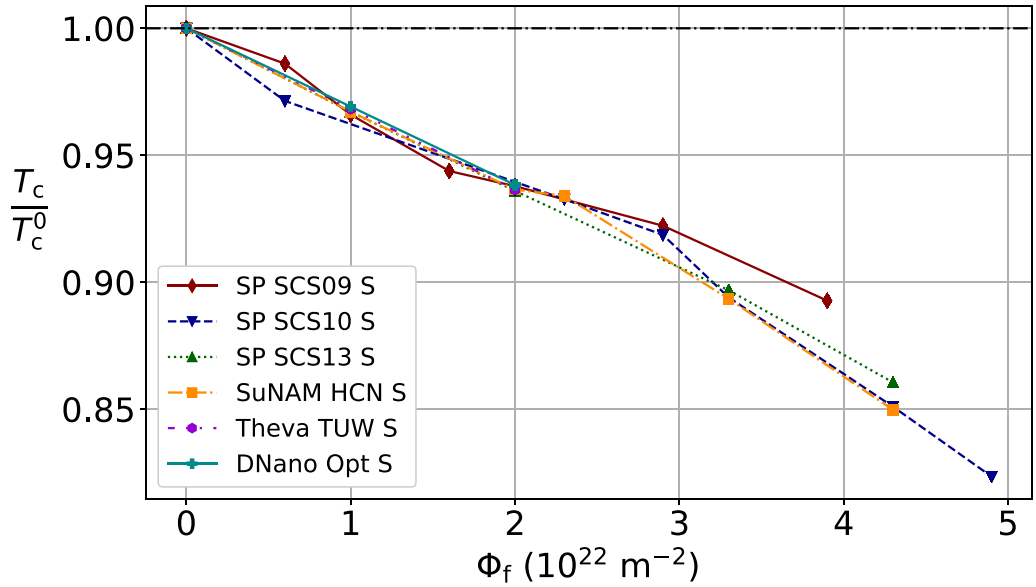

(a) Normalized critical temperature

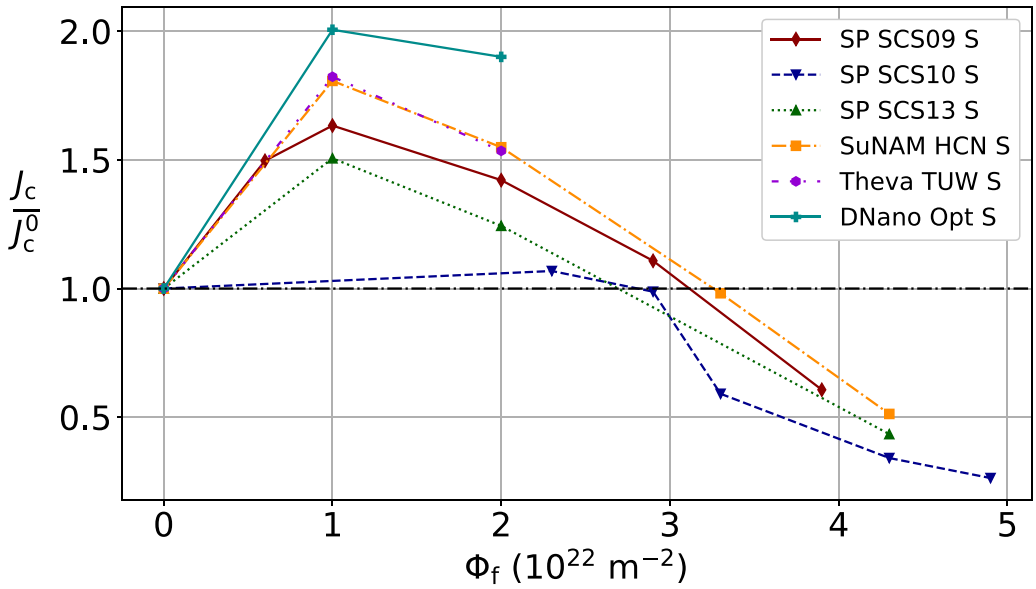

(b) Normalized critical current at 15 T and 30 K

Figure 1. Dependence of superconducting properties on the fast neutron fluence—all data has been evaluated by the authors, however, some measurements were conducted in the scope of the publication [6]; Sample identifiers are given in table 1

better imitate the expected neutron spectrum at the coils of a future fusion power plant [20], which is predicted to contain little to no thermal neutrons. This measure was taken since the irradiation of samples containing gadolinium with the full fission reactor spectrum was observed to produce high defect densities even at low fluences [18]. In irradiation experiments with neutron fluences of up to 10^{22} m^{-2} this effect strongly suppressed T_c and J_c in GdBCO CCs compared to YBCO samples [21]. This results from the high absorption cross section of two gadolinium isotopes. When a neutron is absorbed, one of the following capture processes occurs: ^{155}Gd $\rightarrow ^{156}$Gd* and ^{157}Gd $\rightarrow ^{158}$Gd*. In both cases, the gadolinium enters an excited state, which decays by the emission of a γ, transferring 29–33 eV of recoil energy to the primary knock on atom (PKA) [18]. In addition to knowing the energy range, the well defined position of the PKA Gd involved in this process allows us to perform standard MD collision cascade simulations [22] to identify the different species of resulting defects and to estimate the probability of their formation.

Defects are subdivided in two rough classes in this study, namely large defects, also called collision cascades introduced by fast neutrons with energies >100 keV [15], which upon collision with the crystal lattice deposit enough energy to leave behind an amorphous defect. Under the second class, the small defects, we subsume all defects that do not completely destroy the local order of the crystal lattice. These defects are induced by the neutron capture reactions mentioned above, direct collisions of neutrons ($E_{\mathrm{kin}} \sim 100\,\mathrm{eV}$—$100\,\mathrm{keV}$) and by ionised atoms (e.g. low energy PKAs) colliding with other atoms of the lattice. The latter two processes also occur in the shielded samples and lead to the build up of small defects.

The experiments were conducted on samples which were pre-characterised in their pristine state to ensure the comparability of results avoiding sample to sample variation. The investigated samples were divided into two sets. One was irradiated with the full reactor spectrum and the second was shielded from slow neutrons with an energy below 0.55 eV by wrapping the samples into a 0.5 mm thick cadmium foil, which proved to be effective in a prior study [12].

The samples were prepared for irradiation by placing them into a quartz tube, which was pumped to a vacuum of 0.1 mbar and thereafter flushed with 1 bar helium. This procedure was applied to reduce residual liquids and gases potentially becoming aggressive during irradiation to a minimum. The thus prepared sample containers were welded shut and placed in an aluminum capsule for irradiation. The effectiveness of this procedure was validated after the irradiation: the typical discolorations of the copper stabilizer arising from oxidation amplified by neutron irradiation did not occur on samples helium atmosphere.

The irradiation steps were carried out in the central irradiation facility of the TRIGA Mark II research reactor of TU Wien located at the Atominstitut. In this position, the neutron spectrum has two peaks, one at approximately 1 MeV and the second below 0.1 eV. The flux density sums up to $6.1 \times 10^{16}\,\mathrm{m^{-2}\,s^{-1}}$ for thermal neutrons with an energy $E_{\mathrm{kin}} < 0.55\,\mathrm{eV}$ and $7.6 \times 10^{16}\,\mathrm{m^{-2}\,s^{-1}}$ for fast neutrons with an energy greater than 0.1 MeV [23]. Recent measurements of the fast flux after the core renewal showed a decrease by 55% compared to the published data. Therefore, the fast neutron fluence was quantified in each irradiation step by adding Ni foil to the irradiation capsules and measuring the activity of ^{58}Co following the transmutation of ^{58}Ni by the capture of high energy neutrons.

One sample in this study, denoted with SP SCS09 P, was irradiated to a cumulative fluence of $4 \times 10^{20}\,\mathrm{m^{-2}}$ with 1.2 MeV protons at MIT. The copper layer was removed for proton irradiation and a $2 \times 0.1\,\mathrm{mm^2}$ wide bridge was laser-cut into the surface. Only the bridged area was thereafter irradiated at room temperature, the full details are explained elsewhere [24].

2.2. Samples and characterization

A complete list of all sample identifiers used in the overview figures 1(a) and (b) is given in table 1. The main focus of this work, however, lies on the two samples SuperPower SCS4050 2009 and SuNAM HCN04150. Both samples are based on GdBCO with a 1 μm and 1.35 μm thick superconducting layer, respectively. These tapes have no added artificial pinning centers and exhibit high pristine critical temperatures of approximately 93 K (SP SCS4050 2009) and 93.5 K (SuNAM HCN04150). The behavior of these tapes under fast neutron irradiation is very similar, see figure 1(b), which is why these samples were chosen to compare how different irradiation techniques influence the recovery achievable by annealing. Our experiments were conducted on 27 mm long samples, which were cut from the provided commercial tapes.

Table 1. Sample identifiers, S - shielded sample, U - unshielded sample, P - 1.2 MeV proton irradiated; SP is short for the supplier SuperPower.

Identifier	Tape
SP SCS09 U	SP SCS4050 2009
SP SCS09 S	SP SCS4050 2009
SP SCS09 P	SP SCS4050 2009
SP SCS10 S	SP SCS4050 2010 AP
SP SCS10 P	SP SCS4050 2010 AP
SP SCS13 S	SP SCS4050 2013 AP
SuNAM HCN S	SuNAM HCN04150
Theva TUW S	Theva TUW007
DNano Opt S	DNano Optrium Ni9-04

The tape supplied by SuNAM (HCN04150) are based on a Hastelloy substrate. The GdBCO superconductor is deposited by the reactive co-evaporation by deposition and reaction' method. The superconducting thin film is thereafter coated with 1 μm of silver and stabilized with a copper layer. All annealing data presented in this study on the SuNAM tape has been previously published [8].

The SCS4050 2009 tape was supplied by SuperPower, its superconducting GdBCO layer is applied by the 'metal-organic chemical vapour deposition method' on a 50 μm Hastelloy substrate. The GdBCO film is coated with ~1 μm Ag and stabilized electrically by a copper layer [25, 26]. To texture the REBCO superconductor, both tapes rely on a thin MgO layer which was deposited with the ion-beam-assisted deposition technique.

The samples were characterised by standard four probe transport measurements (SFPTM) conducted in the helium flow cooled variable temperature insert of a liquid helium cooled 17 T cryostat with the applied field H orthogonal to the tape surface. The critical current density J_c was measured at temperatures ranging from 20 K to 77 K and fields from 0 T to 15 T. J_c was determined by fitting the function

$$U = E_c d \left(\frac{I}{I_c}\right)^n \tag{1}$$

to the measured data. U refers to the measured voltage, I the applied current, d the distance between the voltage taps, E_c the chosen electrical field criterion of $1\,\mu\mathrm{V\,cm^{-1}}$. I_c and n are fit parameters representing the critical current and n-value, respectively.

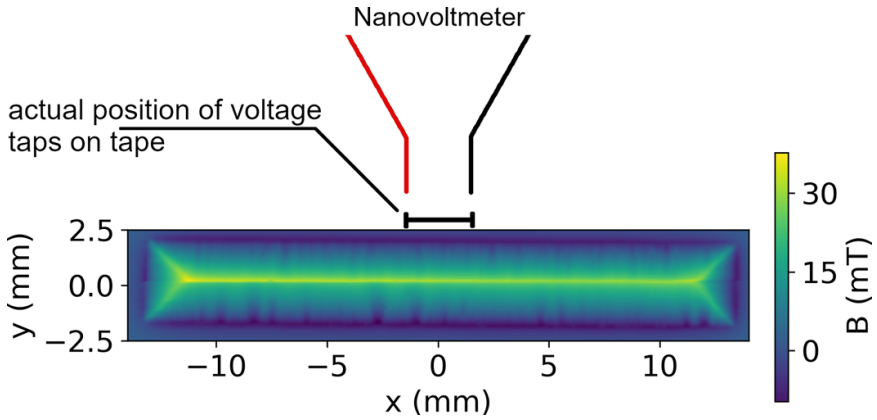

Figure 2. Remnant field of a sample visualized by SHPM.

Dissipation due to poor current contacts can lead to a large error due to the introduction of thermal voltages in these measurements; thus, the temperature of the sample was constantly monitored. A temperature change during the measurement of 0.1 K was defined as upper limit for sufficient thermal stability. This value was experimentally verified and leads to an acceptable error of less than 1% in the critical current measurements.

The resistive transitions were measured by applying 10 mA and fields between 0 and 15 T to the sample and recording the voltage between the voltage taps in delta mode [Keithley Current Source 6220 and Nanovoltmeter 2182A] to eliminate offsets by thermal voltages or chemical potentials. The sample temperature was ramped from high to low temperatures at a rate of only 0.1 K min^{-1} to minimize the lag between the sample temperature and temperature sensor.

In this study, T_c is defined as the temperature where the measured voltage drops to the noise level. Comparing the changes of T_c obtained by this 'offset' method revealed no deviation when compared to the changes of T_c calculated by the conventional tangent criterion. The chosen method, however, proved to render more comparable results for etched and pristine samples.

To ensure the homogeneity of the superconducting layer of all samples, they were investigated by means of scanning Hall probe microscopy (SHPM) [27]. For the SHPM measurement, the samples were submerged in liquid nitrogen at 77 K and fully magnetized by applying a magnetic field perpendicular to the tape surface with a 0.5 T permanent magnet, which leads to the formation of a Bean profile [28]. The resulting remnant field was scanned by a Hall probe with an active area of $30 \times 30\ \mu\mathrm{m}^2$ at a distance of 30 μm from the surface of the sample.

The SHPM setup has a spatial resolution of 50 μm. Samples showing macroscopic damage in the area between the voltage taps were removed from the sample set to improve sample to sample comparability. A scan of a pristine sample can be seen in figure 2, where the position of the voltage taps in the SFPTM setup is also indicated. The method was further used to ensure that changes observed in SFPTM after irradiation are not due to introduced macroscopic damage e.g. cracks, which would be clearly visible in these scans, for an example see appendix C.

Following the irradiation experiments, samples were annealed in a tube oven to test the defect stability. To ensure an ideal doping state, the copper stabilizer was removed by wet chemical etching with sodium persulfate and samples were annealed in pure O_2 at atmospheric pressure. The sample preparation and annealing protocol was kept unchanged to prior work [8] to guarantee comparability of the results. The annealing process was started by heating the sample up to the set annealing temperature T_a at the highest possible rate, which peaks at 2 °C min^{-1} and keeping the temperature constant for 24 h. Thereafter, the samples were cooled to 150 °C at 0.5 °C min^{-1} and then the oven was turned off. The temperature of the samples was measured with a Pt100 sensor to monitor the stability of the process.

2.3. Computational methods

The computational investigation in the present work is aimed at identifying which kind of small, point-like defects might play an important role in the strong suppression of superconducting properties after irradiation with the full fission reactor spectrum (and resulting from neutron capture by Gd). In order to achieve this goal, we develop a workflow that involves classical MD simulations and quantum-mechanical DFT calculations. The MD simulations are used to generate the defective lattice structures of GdBCO expected to be produced in the irradiation experiments. These simulations are performed in relatively small supercells ($3 \times 3 \times 2$ unit cell repetitions, supercell edges ≈12 Å × 12 Å × 24 Å, 234 atoms) which are then used as an input to DFT calculations to obtain the relative stability of different defects, as well as to estimate the electronic properties at the Fermi level. In addition, we extract information on the generated defects from collision cascade MD simulations in larger cells ($16 \times 16 \times 8$ unit cell repetitions, supercell edges ≈60 Å × 60 Å × 95 Å, 26 624 atoms) to enable a more appropriate dissipation of energy.

The MD simulations are used to model the Gd recoil process after the absorption of a neutron and subsequent emission

of a gamma-ray with recoil energy of ≈30 eV. The main ingredients of MD simulations are the interatomic potential used to represent the interaction between atoms, and the simulation methodology.

Since an interatomic potential for GdBCO is presently not available, we employed the potential developed in [19] for YBCO in our MD simulations. The validity of this choice is motivated by the fact that YBCO and GdBCO are very similar materials in terms of chemistry and properties, and we further validate our assumption by showing that the two materials have very similar defect formation energies (see appendix A).

To model the recoil process, we employ the standard methodology for collision cascade simulations [22]: after an initial thermalization of the simulation box and atomic positions (20 ps at constant pressure and temperature employing a Nosè–Hoover thermostat and barostat), constant-energy simulations are performed assigning to a rare earth (RE) atom in the supercell, i.e. the PKA, a velocity corresponding to the recoil energy. The simulations in the small supercells are carried out completely at constant energy, whereas in the larger supercells we rescale the velocities of the outmost layer of atoms in the simulation box every 10 ps to keep them at the experimental temperature (50 °C) and therefore simulate the extraction of heat from the damaged area. This stage of the simulations is carried out with an adaptive timestep [29, 30] for 100 000 steps, corresponding to approximately 100 ps simulation time. For the PKA initial velocity, we consider symmetry-nonequivalent directions in the octant formed by the a, b, and c lattice vectors, sampling uniformly the directions in this space (in spherical coordinates, $\theta, \phi = 0° - 90°$ in steps of 15°, see figure 3). For each direction, we employ initial velocities of 10–50 eV in steps of 10 eV when using the small supercell, and for each velocity vector we carry out 10 statistically independent runs. Since this potential has been shown to have a threshold displacement energy of 33 eV for Y atoms [19], which is very close to the experimental recoil energy of Gd, we employ a range of energies rather than just the experimentally-determined recoil energy to avoid possible inaccuracies in the potential and to obtain a more varied data set of defects. For the MD simulations in the large supercell, instead, we carry out collision cascades with energies close to the experimental recoil energies, namely 30, 35, and 40 eV initial PKA energy, for a total of 430 simulations for each energy. The MD simulations were performed with the LAMMPS software [31], and the defects were detected with the Wigner–Seitz analysis as implemented in Ovito [32].

The DFT calculations are carried out with the Vienna *ab initio* simulation package [33–35] with the projector-augmented wave method [36, 37] and the generalized-gradient approximation of Perdew *et al* [38]. The unit cell of $GdBa_2Cu_3O_7$ is relaxed to obtain the equilibrium, 0 K lattice parameters employing an energy cutoff for plane waves of 600 eV and sampling the first Brillouin zone with a $8 \times 8 \times 4$ Monkhorst-Pack k-point mesh [39]. The atomic positions of the output defect configurations obtained from MD are initially relaxed with the interatomic potential at 0 K, and then rescaled according to the equilibrium lattice parameters obtained from DFT. Further relaxation of atomic positions with forces from DFT ensures that the defect configurations are at a minimum in the potential energy landscape. Since the supercells used here consist of $3 \times 3 \times 2$ repetitions of the unit cell, we employ a less dense k-point mesh of $3 \times 3 \times 2$ for the sampling of the Brillouin zone. The final, relaxed structures are then used to calculate the formation energy of the Frenkel pairs as $E^f(\text{defect}) = E(\text{defect}) - E(\text{ideal})$ and the DOS, with the latter calculated with the tetrahedron method using a denser $4 \times 4 \times 2$ k-point mesh.

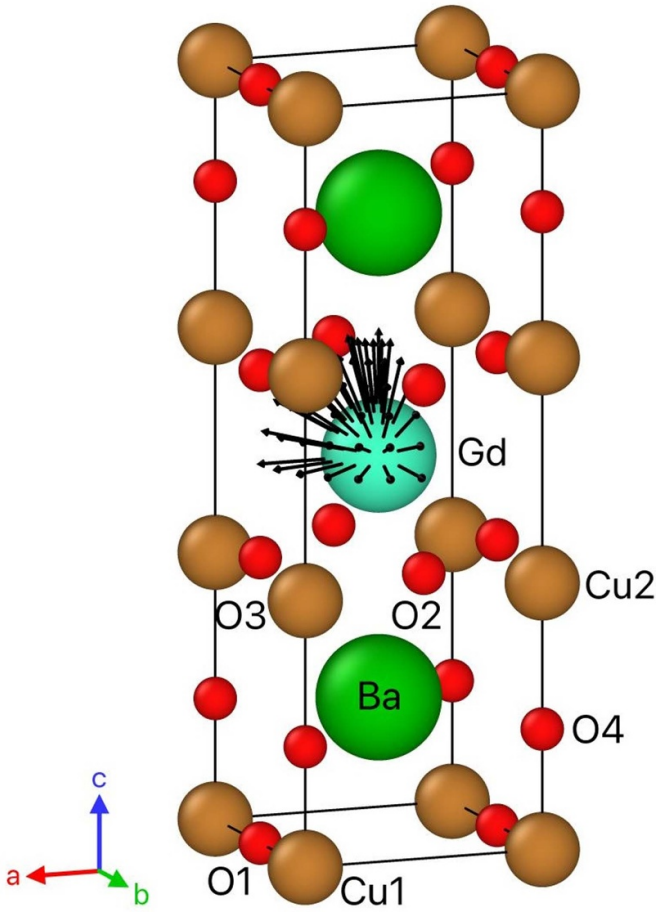

Figure 3. Unit cell of $GdBa_2Cu_3O_7$ (Gd cyan, Ba green, Cu brown, and O red). Arrows indicate the initial direction of the velocity of the RE atom in the MD simulations (black arrows). Image generated with Ovito [32].

3. Results and discussion

Irradiation is known to reduce the critical temperature in d-wave superconductors, due to the pair breaking effect of the newly introduced defects. It was shown in prior studies that the degradation of T_c is linear with fast neutron fluence [6]. In this study, we observed the same linear behavior as well, however, samples irradiated with the full reactor spectrum showed an approximately 15 times larger degradation at the same fast neutron fluence compared to samples shielded with cadmium, which is shown in figure 4. Furthermore, our MD simulations show that a large number of point like defects are formed by

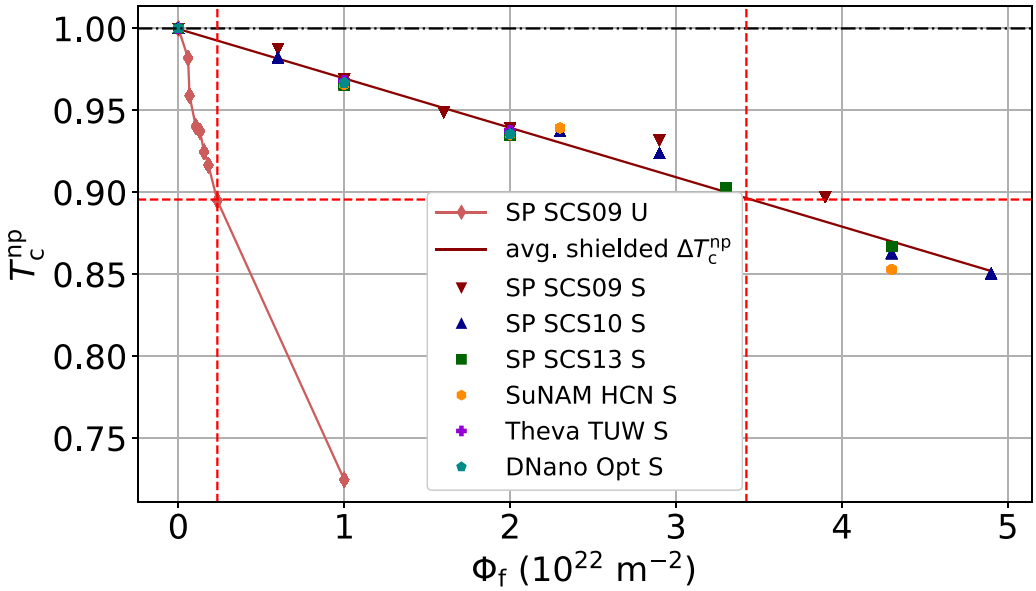

Figure 4. Suppression of T_c by fast and slow neutron irradiation; unshielded (U), shielded (S).

the recoil of the gadolinium nucleus, which is in agreement with the large T_c degradation rates we experimentally observed in unshielded samples.

In GdBCO based samples irradiated with the full reactor spectrum, small defects are induced from both the n—γ reactions and the collision of fast and epithermal neutrons. Since the production of small defects by neutrons colliding with the lattice scales linearly with fluence, their density in the unshielded samples is 15 times lower than in the shielded ones at the same ΔT_c. The contribution of small defects and cascades from the collisions of neutrons with the lattice to the degradation of T_c in unshielded samples can therefore be assumed to be in the range of $\frac{100}{15}\%$, while the small defects induced by n—γ reactions cause the remaining $\sim$93%.

Furthermore, in a prior study, additional defect formation processes induced by neutrons $E_{kin} < 0.55$ eV besides the n—γ reactions were ruled out by shielding YBCO CCs from slow neutrons with cadmium and gadolinium foils. The superconducting properties after irradiation were then compared to data of YBCO based samples irradiated with the full reactor spectrum and no deviation was observed [12]. Consequently, the introduction of small defects in GdBCO by the neutron capture reactions, which are studied in this work with MD simulations, dominates the irradiation induced change of the superconducting properties.

3.1. Irradiation experiments

The stronger T_c suppression by a factor of $\sim$15 in GdBCO based samples irradiated with the full reactor spectrum compared to those irradiated with a cadmium shield is visualized in figure 4. To allow for better data comparability the critical temperature was normalized to its pristine value T_c^p

$$T_c^{np} = \frac{T_c}{T_c^p}. \tag{2}$$

The vertical red lines in figure 4 indicate the fast neutron fluences required to obtain a T_c degradation of about 9 K in shielded and unshielded samples. Furthermore, it was observed that the measured T_c at 10^{22} m^{-2} shows a deviation from the linear trend in the unshielded samples. This matches well the expected behavior at high fluences, since the abundance of the ^{157}Gd and ^{155}Gd isotopes is steadily decreasing with increasing fluence. At the highest fluence point (10^{22} m^{-2}) of the unshielded sample, we estimate the concentration of the isotope ^{157}Gd being reduced by roughly 20% and the isotope ^{155}Gd by 5% leading to a reduction of the n—γ reaction probability. Considering the thermal flux, cross sections of the Gd isotopes and approximate defect formation probability of $\sim 1-2$ per capture reaction calculated by MD simulations, see 3.2, we estimate the n—γ reaction to roughly produce 0.3–0.6 mdpa per 10^{21} m^{-2} of fast neutron fluence corresponding to a measured degradation of T_c by 4.2 K. It has to be emphasized at this point, that the dpa which are estimated by MDS are stable displacements since recombination is accounted for. To put this into perspective, the damage done to shielded samples was calculated to be in the range of approximately 1.3–5 mdpa per 10^{22} m^{-2} [4, 5], leading to a measured T_c suppression of $\sim$3 K. The significantly lower T_c suppression per mdpa of 0.6–2.3 K in fast neutron irradiation experiments compared to $\Delta T_c/\text{mdpa} = 7-14$ K induced by n—γ reactions in GdBCO samples, shows clearly that not only the dpa, but the type of defect and distribution significantly influences the degradation of the superconducting properties. However, since the applied methods are different, the results might deviated from one another and therefore have to be treated with caution.

In this study, we focus on the results of unshielded samples irradiated with a fast neutron fluence of up to 2×10^{21} m^{-2}, corresponding to 0.6 mdpa. Due to the low number of displacements per atom in these experiments, saturation effects and burn up can be neglected and the defect density n_d grows

linearly with the irradiation time while T_c degrades in a linear fashion at the same time. Therefore we may establish the relation $\Delta T_c \propto n_d$ with

$$\Delta T_c = T_c^p - T_c, \tag{3}$$

thus, most data will be plotted against ΔT_c and not the fast neutron fluence Φ_f in this study. This allows a better comparability of the data of shielded and unshielded samples, because our fluence measurement only accounts for the fast neutron flux but not thermal neutrons, which also cause formation of defects via n—γ reactions and thus a degradation of T_c.

From MD simulations we know that a large number of point like defects are formed by the recoil of the Gd nucleus, which is in agreement with the large T_c degradation rates we observed in unshielded samples. While we already established that ΔT_c is proportional to the fluence, and thus the defect density, for both shielded and unshielded samples, we observed a distinct behavior of J_c.

As can be observed in figure 5(b), $J_c(B = 15\,\mathrm{T}, T = 30\,\mathrm{K})$ of a shielded SuperPower SCS4050 2009 sample increases by approximately 60% before starting to degrade and falling below its pristine value at a T_c reduction of $\sim$7.8 K corresponding to a fast neutron fluence of $3.3 \times 10^{22}\,\mathrm{m}^{-2}$. The J_c enhancement can mainly be attributed to the improvement of pinning by large defects introduced to the superconducting layer by fast neutrons. These cascades were shown to have a mean radius of 2 nm, which is comparable to the coherence length $\xi(T = 0) = 1.4\,\mathrm{nm}$ [15].

T_c of the unshielded samples degrades at a 14–15 times faster rate, therefore the pair breaking scattering rate in this sample is larger by about one order of magnitude than in the shielded sample. Nevertheless, The high density of small defects leads to a substantial increase of the critical current at high fields. One observes a lower overall maximum in $J_c(\Delta T_c)$, which is a consequence of these pinning centers being less effective than the large defects introduced by fast neutrons and their stronger degrading influence on T_c.

Unshielded samples contain only 7% of large defect cascades at the same ΔT_c. The unshielded samples increase in J_c, which has to be mainly attributed to the introduced small defects. The maximum in $J_c(B = 15\,\mathrm{T}, T = 30\,\mathrm{K})$ with 30% enhancement is less pronounced and its peak is at a lower ΔT_c compared to the shielded samples of the same type. The fact that the J_c enhancement strongly decreases with increasing temperature confirms that the introduced small defects have a lower pinning energy compared to the larger cascades introduced by fast neutrons. The enhancement of J_c is still significant and could be explained by the formation of multi defect clusters. Our simulations predict these clusters to grow to diameters of up to 10 Å, which would lead to much higher pinning energies than single point defects, see section 3.2.

The peak position of J_c shifts with operation temperature in the shielded sample as shown in figure 5(b). This is due to the pinning energy of large defects being able to compete with the rising thermal energy, while the peak position in J_c of the unshielded sample set does strongly move towards lower ΔT_c for higher operation temperatures and almost disappears at 50 K. This result is in agreement with the defect structures found in MD, since small defects are expected to loose their pinning capabilities at increased temperatures, not being able to compete with thermal energies anymore.

The thorough pre-characterisation allowed us to choose two samples, with practically the same pristine J_c for a direct comparison of the influence of fast and slow neutron irradiation at low fluences. The nearly identical behavior of the samples is shown in the appendix in figure A4. The two points referring to these two samples 30 K are encircled in figure 5. The unshielded sample was irradiated to a cumulative fast neutron fluence of $2.5 \times 10^{20}\,\mathrm{m}^{-2}$ and the shielded sample to $3.36 \times 10^{20}\,\mathrm{m}^{-2}$. The shielded sample is therefore expected to contain approximately one third more large defect cascades than the unshielded sample. Nevertheless, the additional large number of small defects, dominant in the unshielded sample, lead to 3 times the J_c increase (30%) as the cascades in the shielded sample (10%).

The full $J_c(B)$ curves of these two samples are plotted in figure 6 to show that the contribution of small defects to pinning is clearly visible up to 40 K; for the above mentioned reasons, the increase can nott be attributed to larger defects. At 64 K, one observes no increase or reduction of the critical current density of the unshielded sample compared to the pristine value. This may be due to the pinning force enhancement being just enough to compensate the suppression of superfluid density capping the critical current. At lower temperatures, the increased pinning force seems to be the dominating factor, since an increase of J_c is observed.

Figure 7 presents $J_c(\Delta T_c)$ of samples irradiated with different techniques, namely slow and fast neutrons, as well as 1.2 MeV protons. They are found to degrade with nearly the same slope at $\Delta T_c > 6$. This is particularly interesting, since the defect formation processes are substantially different in these three experiments. Especially the proton irradiation is expected to create a large number of randomly distributed point like defects, due to the charged nature of the incident particle and its energy and mass. This result shows that in all these experiments the same mechanism, or even defect type is responsible for the degradation, since all samples, including the unshielded sample, degrade uniformly, as shown exemplary in figure 7 with J_c at $T = 30$ K and $B = 15$ T. This plot visualizes the influence of small defects on the lifetime of CCs in radiation environments.

In order to further study the influence of slow and fast neutron irradiation on the distribution of different defects in the superconductor, also called the pinning landscape, the irreversibility field up to 15 T was measured for shielded and unshielded samples, see figure 8. The irradiation with fast neutrons ($\Phi_f = 2 \times 10^{22}\,\mathrm{m}^{-2}$) introduces new pinning centers, increasing the irreversibility field at high fields. The introduction of small defects by irradiation with thermal neutrons, on the other hand, only leads to a degradation. In order to visualize these results, two pairs of curves with almost the same T_c degradation were chosen for 8.

The pair of curves exhibiting the lower T_c degradation of approximately 6 K, shows that the slope of the irreversibility lines (IL) are quite distinct. While the unshielded sample

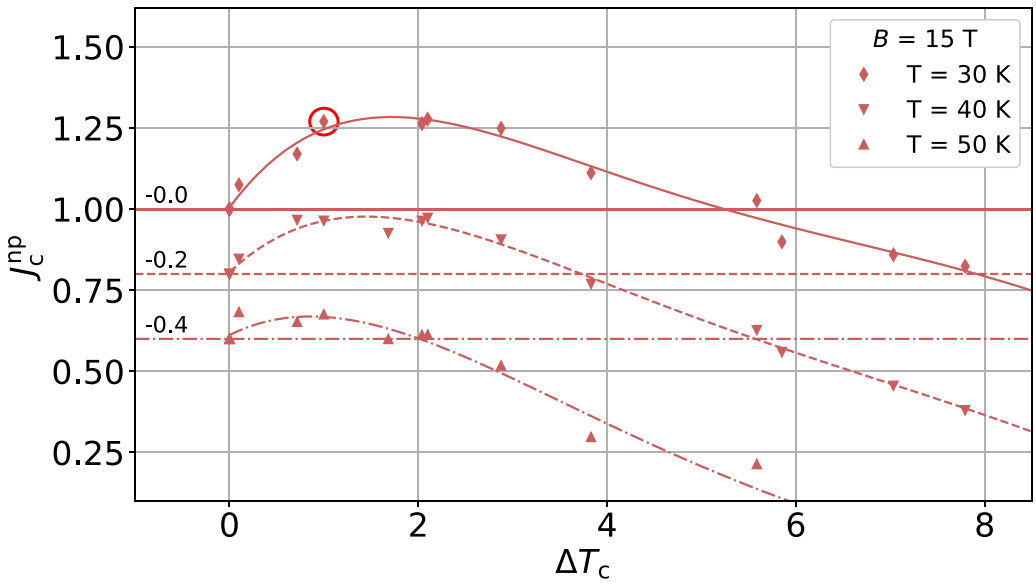

(a) Unshielded sample

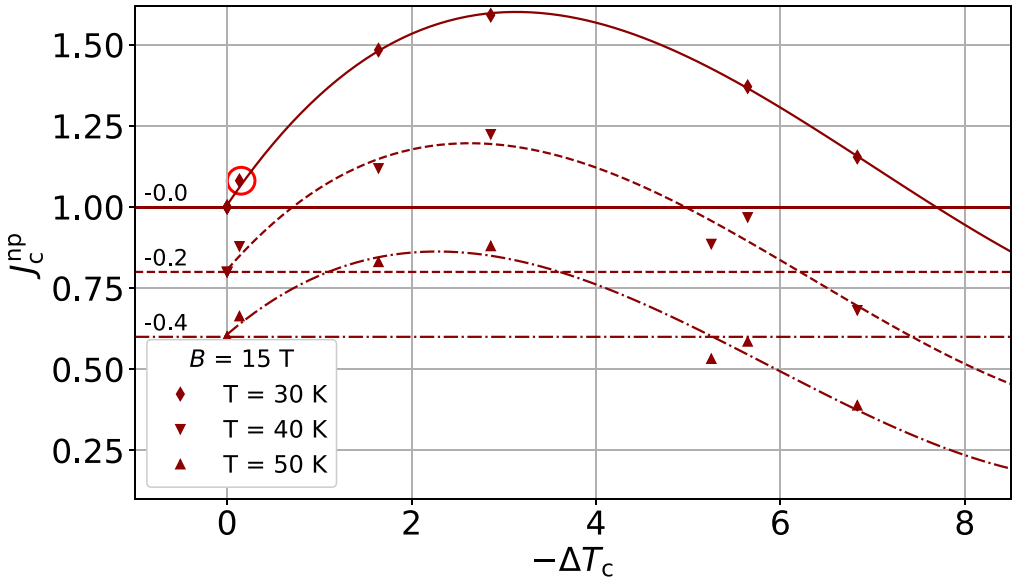

(b) Shielded sample

Figure 5. Influence of neutron irradiation on J_c at 15 T–30 K, 40 K and 50 K; the drawn lines serve to visualize the position of the peak critical current.

shows a similar slope as the pristine curve but shifted to lower temperatures, the slope of the shielded IL increases, which agrees with the introduction of beneficial defects to the preexisting pinning landscape. The thermal neutrons on the contrary only introduce small defects, however their pinning energy cannot compete with the high thermal energies near the irreversibility field. Focusing on the second pair of curves shows that at higher fluences the slope of the fast neutron irradiated sample is reduced, which leads to a tilting backwards of the IL, towards the pristine form. This indicates that the condensation energy gained by pinning a flux core on a defect is reduced at higher fluences, either due to the overall loss of superfluid density, or the degradation of the interface between pinning defects and the undisturbed lattice. The interfacial strain is known to have a strong influence on the pinning force [40]. It is conceivable that the migration and clustering of small defects at these interfaces lead to a change of the interfacial strain and thereby to a reduction of J_c. Since the curves approach each other at high fluences, one may assume that the degradation is determined by the same mechanism in both samples.

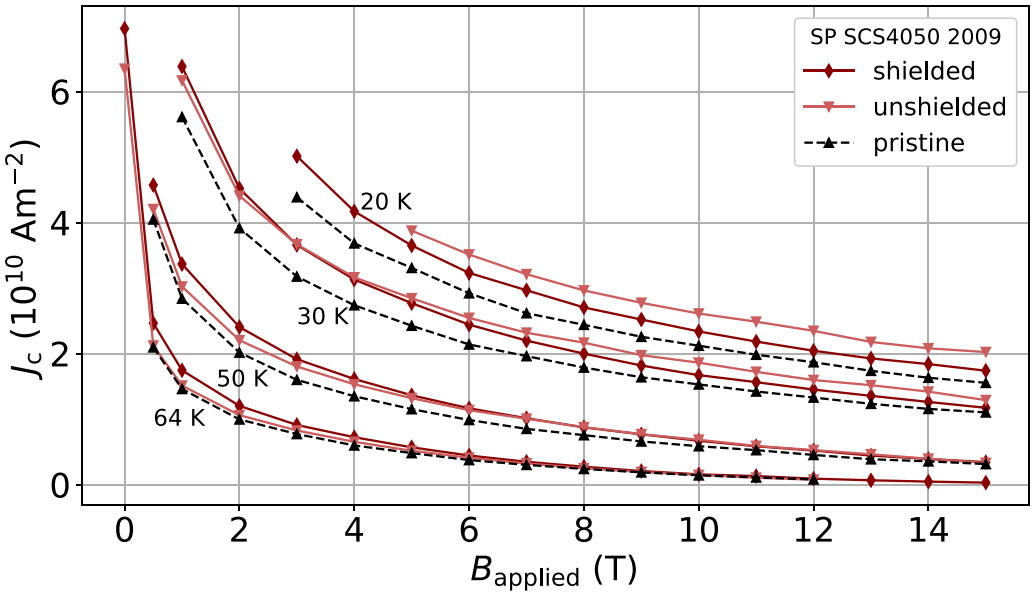

Figure 6. $J_c(B)$ curves of shielded, unshielded and pristine samples at 20, 30, 50 and 64 K.

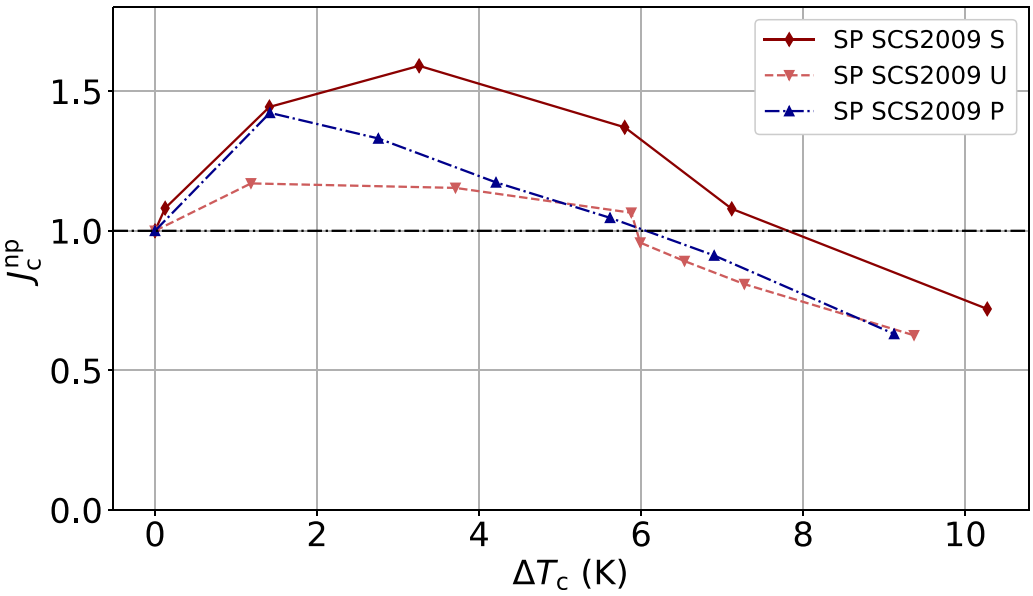

Figure 7. $J_c^{np}(B = 15\ T)$ curves of shielded (S), unshielded (U) and proton irradiated (P) samples at 30 K

Annealing fast neutron irradiated samples at temperatures up to 400 °C in O_2 atmosphere was shown to partially recover their properties [8]. Since defect mobility increases with increasing temperature and distinct defects should exhibit different activation barriers for recombination, annealing provides information on the relevant defects. While for example oxygen should be rather mobile and therefore easy to anneal at lower temperatures, amorphous cascades are only expected to anneal at temperatures close to the melting point of the crystal lattice.

The available critical temperature data was normalized to its pristine value and fitted with the linear function $f(x) = kx + d$, to extrapolate to higher annealing temperatures and to visualize the mean slope of the recovery of T_c in figure 9. Though the samples irradiated with slow neutrons and even more so protons, should lead to a completely different defect size distribution compared to the samples irradiated with fast neutrons, the slope only depends on the reduction of T_c after irradiation, resulting in the observed linear behavior demonstrated in figure 9(b). Since large cascades were shown not to anneal at temperatures up to 400° [15], the recovery only comes from removing small defects and strain in the lattice. The ΔT_c proportionality of the slopes can therefore be explained with a uniform accumulation of the same T_c degrading defect species in all examined irradiation experiments.

Though the here described damage processes to CCs by thermal neutrons will not occur in fusion applications due to the absence of a thermal peak in the neutron energy spectrum,

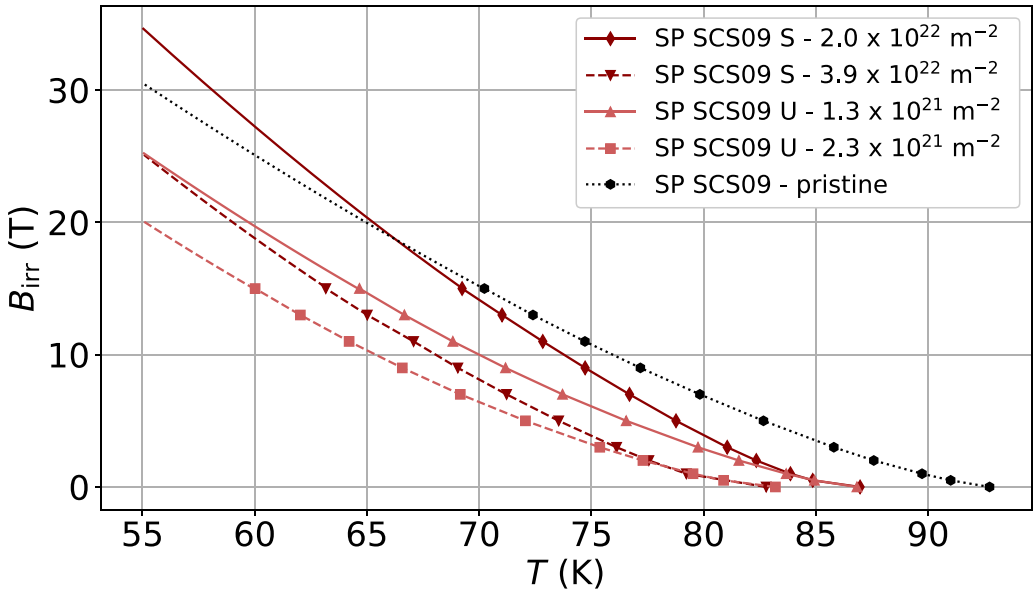

Figure 8. $B_{\mathrm{irr}}(T)$ of a pristine, shielded (S) and unshielded (U) sample

the experimental results clearly show that J_c and T_c of CCs in fast neutron irradiation environments degrade due to the accumulation of small defects.

3.2. Computational modeling of induced defect structures

MD simulations of the recoil process that follows thermal neutron capture show a defect formation probability of 45, 60 and 70% for 30, 35 and 40 eV recoil energy, respectively, considering all PKA directions. As can be seen from figure 10, the vast majority of these defects is O Frenkel pairs (interstitial and vacancy pairs) at all energies, and in particular at $E_k =$ 30 eV, where these are almost the only defects generated. At higher energies, more diverse defects are generated with an increasing relative occurrence as compared to O Frenkel pairs, although their density is still about one order of magnitude lower. For what concerns vacancies, we observe a strong predominance of O1 and O4 vacancies, due to the openness of the structure around the CuO chains, which enables the displacement of atoms from the chain (O1) or from the apical site (O4) into interstitial positions in between the chains.

The increase in total number of defects does not rise linearly with energy due to the fact that the threshold displacement energy for the rare earth element is reached in this range. $E_k = 35$ eV is the closest energy to the recoil energy of Gd, therefore these results are the most relevant for comparison with experiments; nonetheless, the investigation of a range of energies gives a clearer picture of the defect formation process, keeping in mind that the potential might fail in the precise representation of recoil processes that differ of only 5–10 eV. From these results, we obtain an average of 1–2 defects generated per PKA recoil process, as mentioned in section 3.1.

In order to assess the transferability of the interatomic potential in the representation of GdBCO, we carried out similar collision cascades simulations in smaller cells ($3 \times 3 \times 2$ unit cell repetitions), which were then employed as input of DFT calculations. The obtained defect formation energies are shown in figure 11 and selected configurations are compared to formation energies in YBCO in appendix A. As obvious from this plot, the defects involving only O Frenkel pairs have a much lower formation energy than defects involving other species, even when several O Frenkel pairs are present. In the case of defects involving other species, O Frenkel pairs are often present at the same time. Among all the computed defects, two configurations were included manually because they did not result from MD simulations. These configurations are an O Frenkel pair involving an O2 vacancy and an O interstitial in the Gd plane ($E^f = 1.25$ eV) and a swapping of Ba and Gd atoms ($\mathrm{Ba^{Gd}}$-$\mathrm{Gd^{Ba}}$ antisites, $E^f = 1.54$ eV): the latter configuration was included in the set because it was chemically reasonable to display a low formation energy, although it might be dynamically difficult to form because the formation process would involve the displacement of several atoms in a concerted mechanism; the former was included because it has been proposed as an important defect with some theoretical and experimental basis [17], but the interatomic potential predicts it unstable. The formation energies reported here should not be understood as the energy needed to generate the defects in a dynamic process, but rather in a thermodynamic sense at equilibrium conditions. Nonetheless, a high formation energy indicates a highly unfavorable defect configuration, which can be expected to anneal at short timescales, although an estimation of annealing times and temperatures would require knowledge of diffusion barriers and prefactors and it is beyond the scope of the present work.

It is difficult to assess the different pair-breaking potential of these small defects since the superconducting properties of REBCOs cannot be calculated from DFT. In addition, several effects concur in the scattering of Cooper pairs [41] which are currently impossible to calculate from first principles. Nonetheless, we found that the reduction of DOS at the Fermi level correlates well with the experimental reduction in

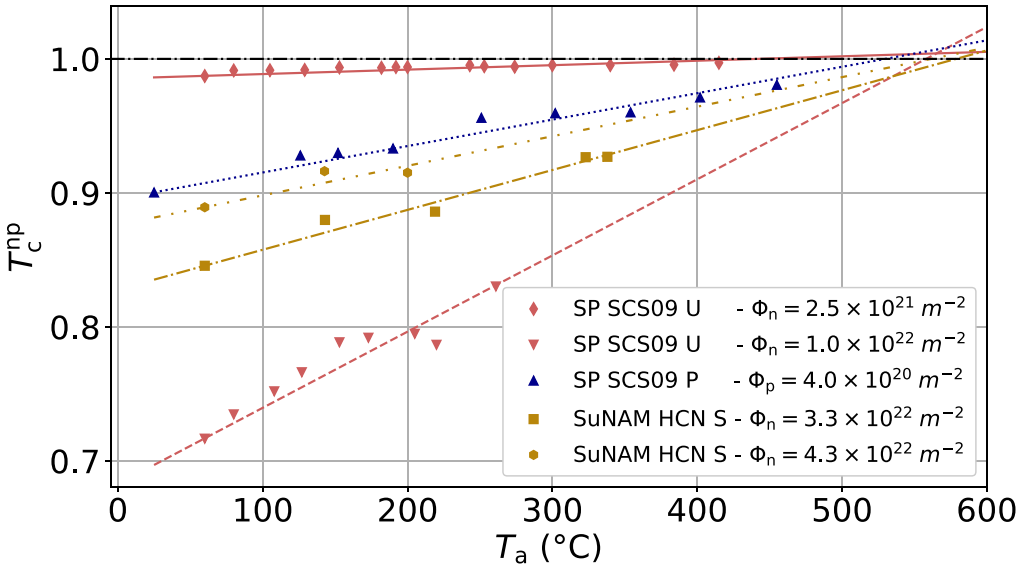

(a) T_c is normalized to its pristine value - a linear fit was used to extrapolate the behavior

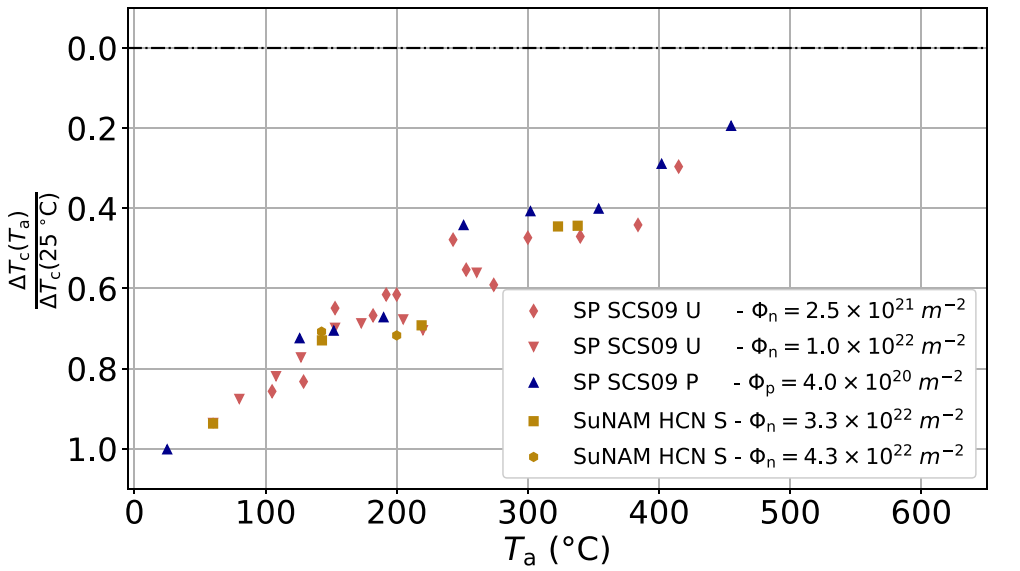

(b) ΔT_c is normalized to its value at $T_a = 25\,°C$

Figure 9. Recovery of T_c as a function of annealing temperature—unshielded (U), shielded (S), proton irradiated (P); data on SuNAM HCN samples from [8].

T_c of YBCO chemically substituted with different elements (see appendix B), as this is strongly correlated with the superfluid density (see, e.g. [42]). We therefore can get hints of which defects have a strong effect on the superfluid density by calculating the projected DOS in the CuO_2 planes and compare it with the defect-free DOS, see figure 12(a). From the present calculations, the Frenkel pair involving an O2 vacancy and an O interstitial in the Gd plane [$O2^v - O^i$(Gd plane), blue line] seems to have a stronger effect on the local DOS of the plane as compared to O1 and O4 vacancies with O interstitial in between the CuO chains (orange and green lines, respectively), and comparable to the effect of a Gd^{Cu} antisite in the CuO_2 plane (pink line). Structural models of these defects can be seen in figure 12(b). This last defect can be intuitively understood as the most disruptive in terms of local DOS of the plane, so it is interesting to notice that the $O2^v - O^i$(Gd plane) defect is as effective in suppressing the DOS at the Fermi level. Of course, in a macroscopic sample, the frequency of occurrence of a defect is also very important, therefore the $O1^v/O4^v - O^i$(chain) defects could play an important role in the worsening of superconducting properties just because they are more common. We would like to notice in passing that the Gd atom is magnetic, however magnetic impurities are not expected to be stronger Cooper pair breaking than

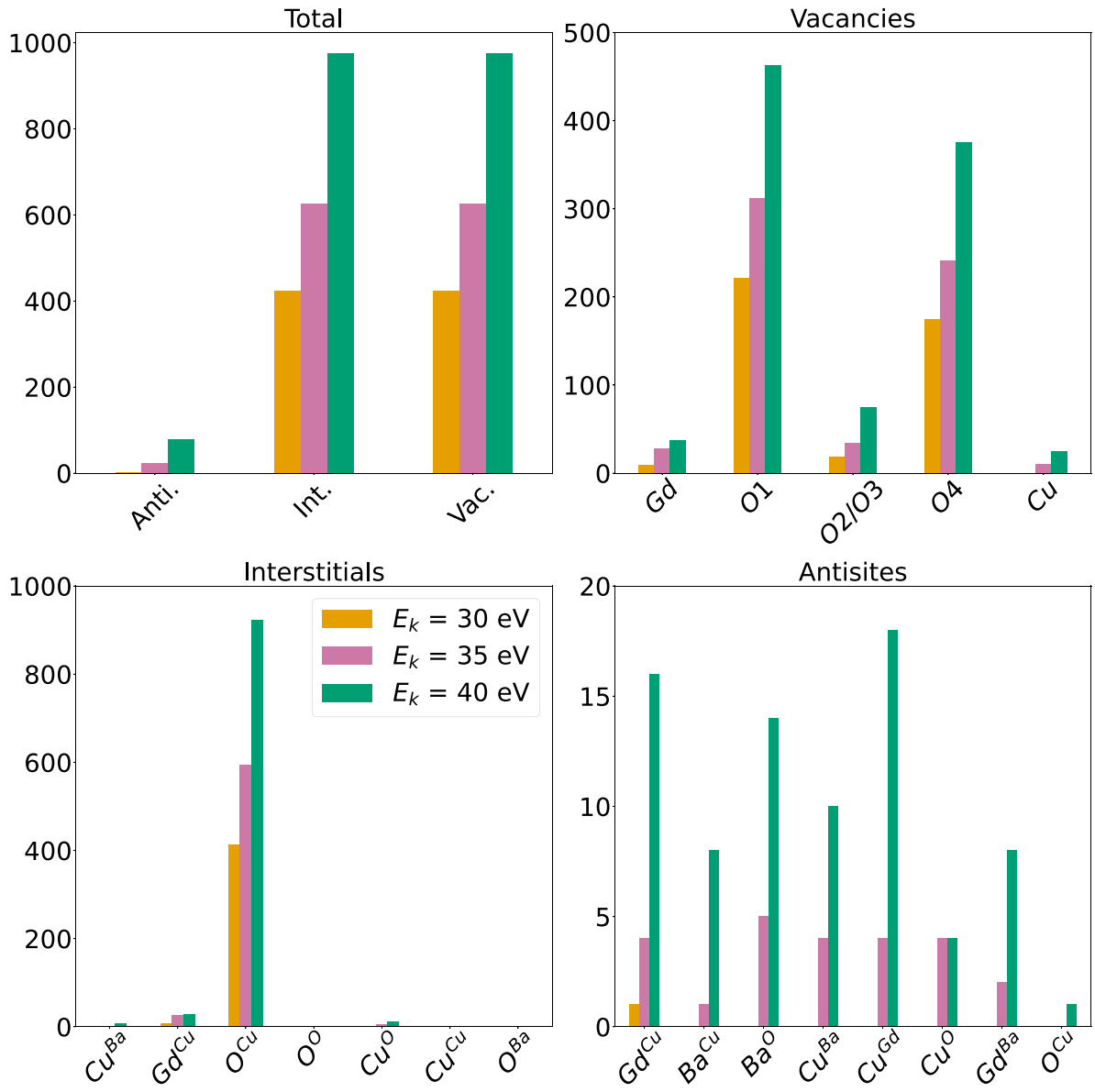

Figure 10. Number of (a) total, (b) vacancy, (c) interstitial, and (d) antisite defects for different involved sites and atom types generated in the 430 collision cascade MD simulations at each energy. The nomenclature for interstitial and antisite defects is $\langle$ atom type $\rangle^{\langle \text{site type} \rangle}$. Notice the different scales for each subplot.

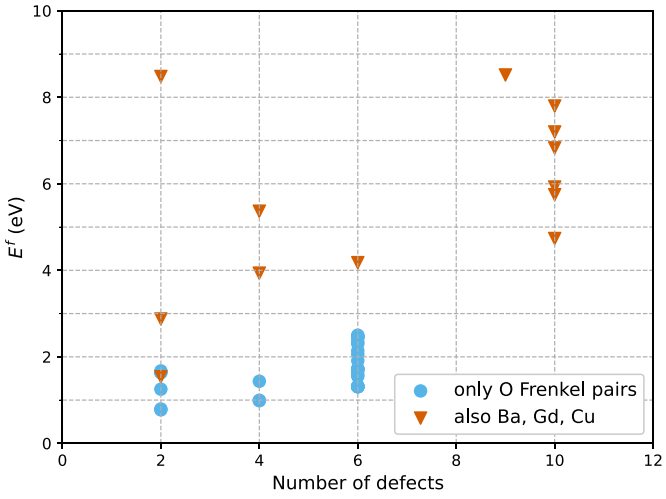

Figure 11. Defect formation energy from DFT in GdBCO for configurations involving different numbers of displaced atoms. Blue circles are defects involving only O Frenkel pairs, orange triangles involve also other species

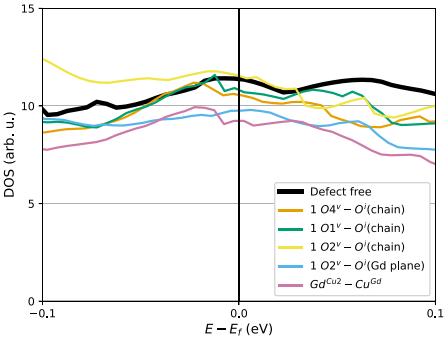

(a) The position of the O interstitial atoms is reported in parentheses. For the antisite, the nomenclature is the same as in figure 10.

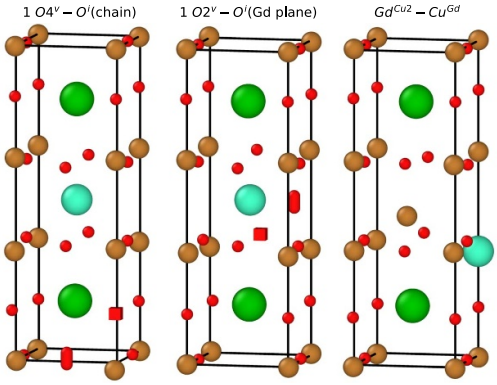

(b) $1O4^v - O^i$(chain), $1O2^v - O^i$(Gd plane), and $Gd^{Cu2} - Cu^{Gd}$ defect configurations (respectively) represented in the conventional cell of GdBCO for clarity purposes. Cubes are vacancies, whereas spherocylinders are interstitial atoms. The color code is the same as in figure 3.

Figure 12. Projected DOS of CuO planes for selected defect configurations and examples of structural models.

non-magnetic ones in d-wave superconductors [41]. Further DOS calculations with an O2 vacancy and an O interstitial in between the CuO chain (yellow line in figure 12(a)) show a negligible effect on the local DOS (they still could be efficient pair breaking scattering centers), therefore stressing the importance of the O interstitial in the Gd plane which can be understood as drawing out electrons from the CuO_2 plane. In addition, we calculated the DOS in the planes in the presence of several O1 and O4 vacancies and O interstitials in between the chains (not shown), with distances between defects of more than one *a* lattice vector, but the effect on the DOS in the CuO_2 planes is comparable with the single Frenkel pairs.

All the computational results up to this point are connected with the decrease of T_c in the system, but we have shown in section 3.1 that there is an effect of small defects also on J_c. For this reason, we analyzed the defect clusters generated in our MD simulations considering a cutoff of 3.8 Å (wider spaced defects are not counted), approximately corresponding to the *a* lattice parameter, and the results are shown in figure 13. With this cutoff, defects belonging to adjacent layers in the structure are counted as part of the same cluster, which should be a good criterion for the definition of a cluster in this system. This choice is also motivated by the fact previously mentioned that Frenkel pairs placed in different layers in the cell do not strongly affect the DOS of the other layers. We observe that single defects and pairs of defects are the most frequent, although clusters with up to 10 defects are quite common (figure 13(a) top). Typical gyration diameters of the clusters are often in the order of 10 Å, suggesting that these clusters might be involved in pinning and therefore increase of J_c. It should be noted that the clusters considered here can encompass also several atoms in ideal positions (see shaded areas in figure 13(b)), therefore they should not be thought as completely amorphous cascades resulting from fast neutrons as seen in TEM (transmission electron microscopy) images [14], also hinting at a lower pinning power.

4. Conclusions

Our experimental results show clearly the influence of small defects on the superconducting properties of REBCO. Though in fusion devices capture reactions of thermal neutrons are of no concern due to the low abundance of low energy neutrons, small defects are certain to form from other collision reactions and lead to the same degradation, only at a slower rate. GdBCO samples were irradiated both, with the full reactor spectrum including low energy neutrons ($E < 0.55$ eV), as well as shielded by cadmium foil in typical irradiation experiments to protect the samples from degradation induced by capture reactions. $T_c(\Phi_f)$ and $J_c(\Phi_f)$ of unshielded samples were found to degrade 14–15 times faster when compared to samples irradiated in shielded conditions. The fast degradation of unshielded samples stems from n—γ reactions of the naturally occurring ^{155}Gd and ^{157}Gd isotope exhibiting large absorption cross sections for thermal neutrons. This capture reaction transfers 29–33 eV of recoil energy to the Gd PKA, leading to the introduction of small defects.

MD simulations of this process for 30, 35 and 40 eV of recoil energy predict a high defect formation probability of 45%, 60% and 70% respectively. Not distinguishing between the diverging influence on the superconducting properties of different defects and only taking recoil energies of 30–35 eV into account which are closest to the energies derived from experiments, our simulations predict the formation of approximately 1–2 defects per incident neutron. Considering the neutron spectrum of the TRIGA Mark II fission reactor, we estimate the introduction of 0.3–0.58 mdpa

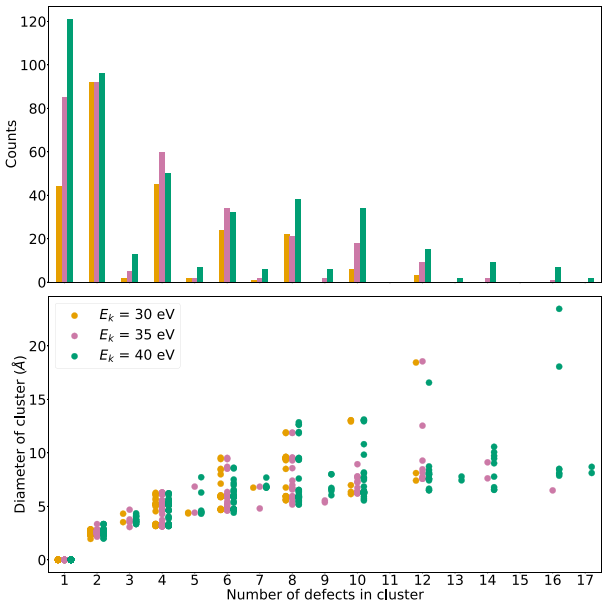

(a) Number of occurrences of defect clusters (top) and their gyration diameter (bottom) as a function of the number of defects in the cluster for different investigated energies.

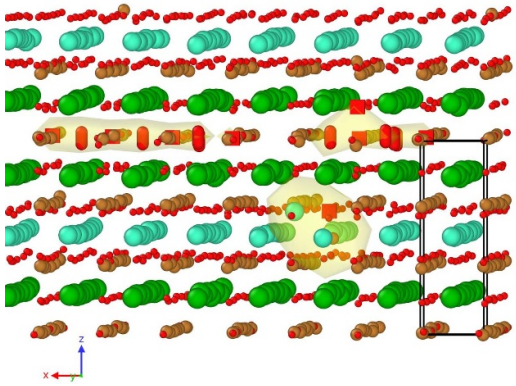

(b) Example of 3 defect clusters generated by the same collision cascade. The shaded volumes define the different clusters, although their dimensions are not directly connected to the gyration diameters. The unit cell is shown as a reference dimension.

Figure 13. Properties of defect clusters from MD simulations and an example of such clusters.

per $\Phi_f = 10^{21}\,m^{-2}$. The absorption of low energy neutrons in unshielded tapes causes a suppression of ΔT_c of 7–14 K per mdpa. This compares to only $\Delta T_c/\text{mdpa} = 0.6 - 2.3$ K in samples irradiated with fast neutrons. The 3–23 times stronger degradation per mdpa of unshielded GdBCO samples underlines the significantly diverging influences of different defects on the superconducting properties.

Results from MD simulations show the most probable defects to form are oxygen O1 and O4 vacancies, with the displaced oxygen most commonly forming an interstitial in the CuO chains. Additionally, O2/O3 vacancies were found to occur, but at a 5–9 times lower abundance. In our simulations, antisites only start to form at energies larger than 30 eV of recoil energy. In order to determine the influence of different defect types on the superconducting properties, the reduction of the local DOS at the Fermi level was calculated using DFT. The defects found to have the highest abundance ($O1^v/O4^v - O^i$(chain)) show the lowest influence on the DOS; however, their large number might still lead to a strong suppression of the superconducting properties. The $O2^v - O^i$(Gd plane) was found to be the oxygen defect with the highest influence on the DOS and comparable to an Gd^{Cu} antisite defect. This defect is so disruptive to the local DOS not because an oxygen atom is removed from the superconducting CuO_2 plane, but because an interstitial oxygen is placed in the Gd plane. The influence of Frenkel pairs on the DOS was found to be spatially limited to approximately one a lattice vector, however defect clusters with a size of up to 10 Å were found to be quite common in our MD simulations. This could provide an explanation for the unexpected high increase of ∼30% of J_c at 30 K and 15 T observed in our unshielded samples.

The defects predicted here to be responsible for the degradation of the unshielded GdBCO samples are likely responsible in general for the degradation of samples in radiation environments. We derive this from the almost identical degradation rates of $J_c(\Delta T_c)$ at all fields and temperatures in our samples, which were irradiated differently, with fast neutrons, slow neutrons or 1.2 MeV protons. Furthermore, we observed the recovery of $T_c(\Phi_f, T_a)$ to only be dependent on the defect density upon annealing, which indicates that defects with the same activation barrier and influence on the superfluid density anneal in all investigated samples.

Data availability statement

The data cannot be made publicly available upon publication because they are not available in a format that is sufficiently accessible or reusable by other researchers. The data that support the findings of this study are available upon reasonable request from the authors.

Acknowledgment

This work has been carried out within the framework of the EUROfusion Consortium, funded by the European Union via the Euratom Research and Training Programme (Grant Agreement No 101052200 - EUROfusion). Views and opinions expressed are however those of the author(s) only and do not necessarily reflect those of the European Union or the European Commission. Neither the European Union nor the European Commission can be held responsible for them.

The authors acknowledge TU Wien Bibliothek for financial support through its Open Access Funding Programme.

The authors would furthermore like to acknowledge SuperPower, SuNAM, Faraday Factory, Theva and DNano for supplying the samples used in this work. D G acknowledges

financial support from the Swedish Research Council (VR) through Grant No. 2023-00208.

The computations were enabled by resources provided by the National Academic Infrastructure for Supercomputing in Sweden (NAISS) at the National Supercomputer Centre (NSC), Linköping University, and at the PDC Center for High Performance Computing, KTH Royal Institute of Technology, partially funded by the Swedish Research Council through Grant Agreement No. 2022-06725. DG also would like to acknowledge Davide Sangiovanni for useful discussions. DT and FL acknowledge partial support by the European Cooperation in Science and Technology (COST) action CA19108: 'High-Temperature Superconductivity for Accelerating the Energy Transition', by the Italian Ministry of Foreign Affairs and International Cooperation, Grant Number US23GR16, and by Eni S.p.A.. D T also acknowledges that this study was carried out within the Ministerial Decree no. 1062/2021 and received funding from the FSE REACT-EU—PON Ricerca e Innovazione 2014-2020.

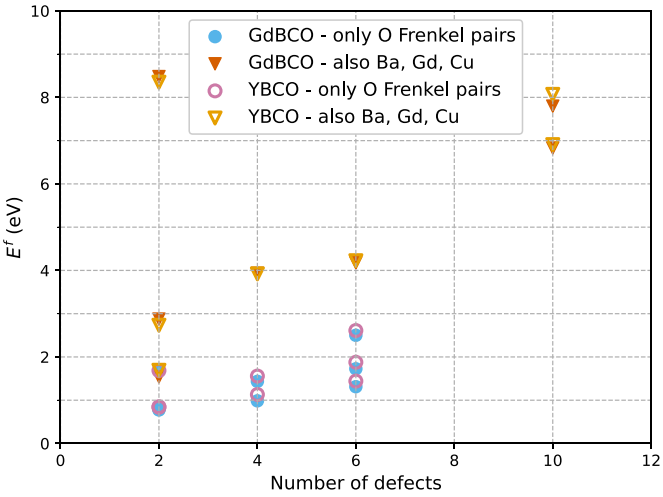

Figure A1. Defect formation energy from DFT in GdBCO and YBCO for configurations involving different numbers of displaced atoms. Blue full (pink empty) circles are defects involving only O Frenkel pairs, orange full (yellow empty) triangles involve also other species in GdBCO (YBCO).

Appendix A

All REBCOs show similar physical properties, however it is in principle not correct to employ an interatomic potential developed for one system to represent another. Development of an interatomic potential for GdBCO is a long and tedious job which goes beyond the scope of the present work, we therefore employed the potential developed by Gray *et al* [19] for YBCO in the representation of GdBCO. To motivate our choice, we calculate the formation energy of selected defects calculated with DFT for the two systems: this is a good benchmark of the transferability of the potential, since it was shown to reproduce fairly well the Frenkel pair formation energies in YBCO [19] and we are only interested in defect properties for what concerns the classical MD simulations. The resulting formation energies, shown in figure A1, are indeed very similar between the two systems, with differences in formation energies ranging between 0.4 and 15% of the GdBCO values.

Appendix B

We present in this section DFT calculations of the DOS of the CuO_2 planes where a Cu atom has been substituted with another transition element (Fe, Ni, and Zn). The atomic coordinates of the substituted systems have been relaxed according to DFT forces, while keeping the lattice vectors fixed as to model a single impurity substituted in a perfect crystal. The results of our DFT calculations are shown in figure A2(a), and the experimental reduction of T_c as a function of composition [43–45] is presented in figure A2(b). Focusing on the lowest concentration ($x \approx 0.0025$), we see that the order of T_c reduction correlates well with the order in our DOS calculations. For higher concentrations of substituting element, we see that T_c for Fe substitution falls below the Ni value, but substitution with Fe is accompanied by a structural transition to tetragonal symmetry which affects even further the superconducting properties of YBCO, and which we do not take into account in our calculations.

Appendix C

The magnetic profile of our samples was scanned with SHPM in liquid nitrogen at atmospheric pressure prior to and after irradiation to exclude that macroscopic damage is responsible

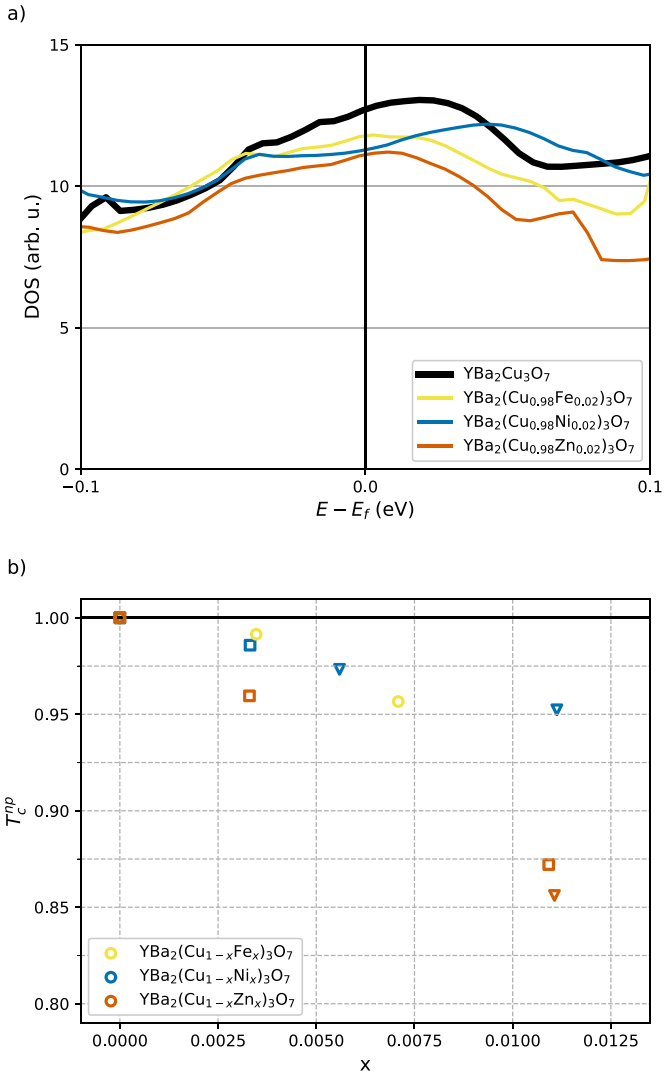

Figure A2. (a) DOS of the CuO_2 planes of YBCO chemically substituted with Fe (yellow), Ni (blue), and Zn (orange) as compared to the pure DOS (black). (b) Experimental reduction of T_c from chemical substitution of Cu with Fe, Ni, and Zn taken from literature (circles: [43], triangles: [44], squares: [45]).

for the change of the superconducting properties observed in SFPTM. One example of such a scan is shown in figure A3, the difference of the maximum magnetization observable in the scan correlate with the suppression of J_c at 77 K in self field.

To directly compare the influence of shielded and unshielded irradiation in section 3.1 two samples with practically identical pristine J_c, at all fields and temperatures, were chosen from the set. The pristine data of these two samples is shown in figure A4.

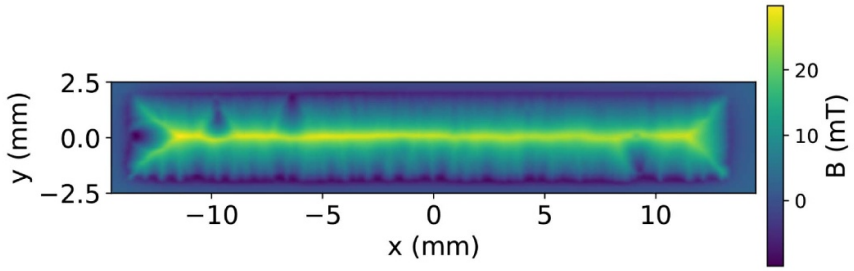

(a) unirradiated sample

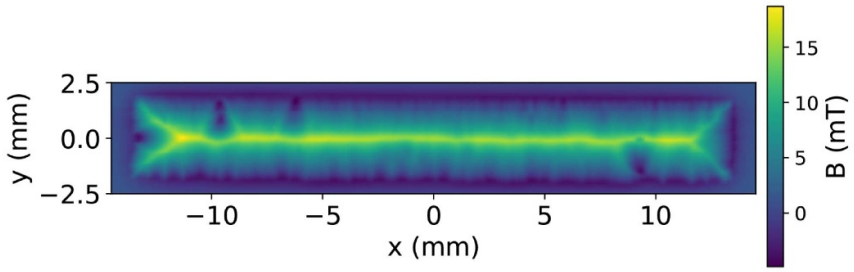

(b) irradiated sample - $\Phi_f = 10^{21}\,m^{-2}$ 8h unshielded

Figure A3. magnetic profile of SP SCS 4050 tape—spatial resolution $50 \times 50\,\mu$m

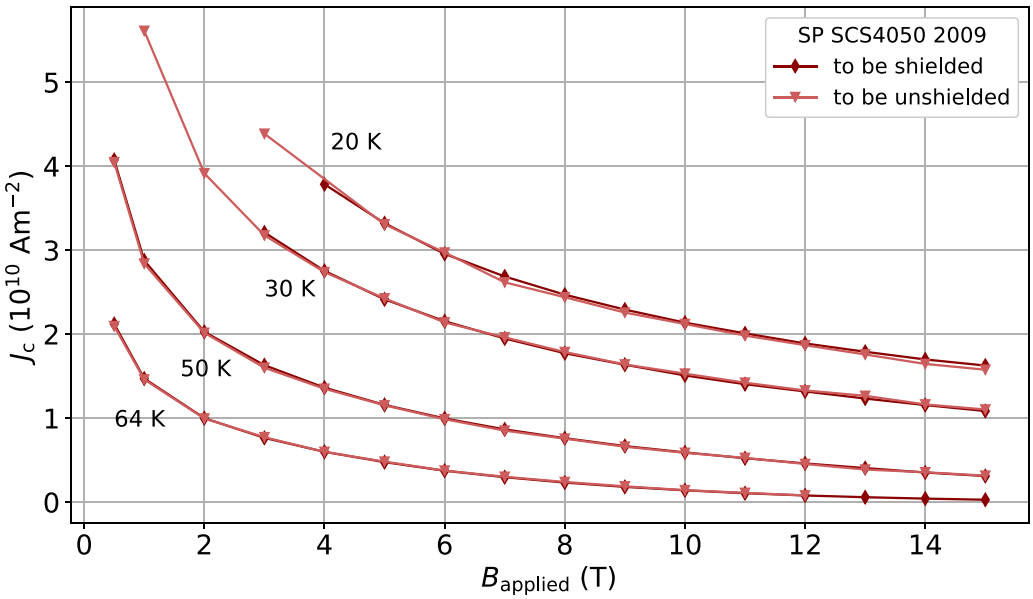

Figure A4. $J_c(B)$ curves of pristine samples

ORCID iDs

Raphael Unterrainer https://orcid.org/0000-0002-8720-9004
Davide Gambino https://orcid.org/0000-0002-7763-7224
Florian Semper https://orcid.org/0009-0003-6212-0657
Alexander Bodenseher https://orcid.org/0000-0002-2959-1962
Daniele Torsello https://orcid.org/0000-0001-9551-1716
Francesco Laviano https://orcid.org/0000-0002-5271-6575
David X Fischer https://orcid.org/0000-0003-2916-8555
Michael Eisterer https://orcid.org/0000-0002-7160-7331

References

[1] Strickland N M 2021 Qualifying high-temperature superconductors for fusion reactors *Supercond. Sci. Technol.* **34** 110502
[2] Meschini S, Laviano F, Ledda F, Pettinari D, Testoni R, Torsello D and Panella B 2023 Review of commercial nuclear fusion projects *Front. Energy Res.* **11** 06

[3] Sorbom B N *et al* 2015 ARC: a compact, high-field, fusion nuclear science facility and demonstration power plant with demountable magnets *Fusion Eng. Des.* **100** 378–405

[4] Torsello D, Gambino D, Gozzelino L, Trotta A and Laviano F 2022 Expected radiation environment and damage for YBCO tapes in compact fusion reactors *Supercond. Sci. Technol.* **36** 014003

[5] Adams K, Iliffe W, Nicholls R J, He G, Diaz-Moreno S, Mosselmans F, Fischer D, Eisterer M, Grovenor C R M and Speller S C 2023 Comparing neutron and helium ion irradiation damage of $REBa_2Cu_3O_{7-\delta}$ coated conductor using x-ray absorption spectroscopy *Supercond. Sci. Technol.* **36** 10LT01

[6] Fischer D X, Prokopec R, Emhofer J and Eisterer M 2018 The effect of fast neutron irradiation on the superconducting properties of REBCO coated conductors with and without artificial pinning centers *Supercond. Sci. Technol.* **31** 044006

[7] Ledda F, Torsello D, Pettinari D, Sparacio S, Hartwig Z, Zucchetti M and Laviano F 2024 3D neutronic and secondary particles analysis on $YBa_2Cu_3O_{7-\delta}$ tapes for compact fusion reactors *IEEE Trans. Appl. Supercond.* **34** 1–6

[8] Unterrainer R, Fischer D X, Lorenz A and Eisterer M 2022 Recovering the performance of irradiated high-temperature superconductors for use in fusion magnets *Supercond. Sci. Technol.* **35** 04LT01

[9] Fuger R, Eisterer M and Weber H W 2009 YBCO coated conductors for fusion magnets *IEEE Trans. Appl. Supercond.* **19** 1532–5

[10] Eisterer M, Fuger R, Chudy M, Hengstberger F and Weber H W 2009 Neutron irradiation of coated conductors *Supercond. Sci. Technol.* **23** 014009

[11] Chudy M, Fuger R, Eisterer M and Weber H W 2011 Characterization of commercial YBCO coated conductors after neutron irradiation *IEEE Trans. Appl. Supercond.* **21** 3162–5

[12] Fischer D X 2019 Effect of neutron radiation damage on coated conductors for fusion magnets *PhD Thesis* Technische Universität Wien (https://doi.org/10.34726/hss.2019.27911)

[13] Radtke R J, Levin K, Schüttler H-B and Norman M R 1993 Predictions for impurity-induced t_c suppression in the high-temperature superconductors *Phys. Rev.* B **48** 653–6

[14] Linden Y, Iliffe W R, He G, Danaie M, Fischer D X, Eisterer M, Speller S C and Grovenor C R M 2022 Analysing neutron radiation damage in $YBa_2Cu_3O_{7-x}$ high-temperature superconductor tapes *J. Microsc.* **2** 3–12

[15] Frischherz M C, Kirk M A, Farmer J, Greenwood L R and Weber H W 1994 Defect cascades produced by neutron irradiation in $YBa_2Cu_3O_{7-\delta}$ *Physica* C **2** 309–27

[16] Eisterer M, Unterrainer R and Fischer D X 2020 PresentationDegradation of the critical currents at high defect concentration *Applied Supperconductivity Conf. 2020* (*Tampa, USA*)

[17] Nicholls R J, Diaz-Moreno S, Iliffe W, Linden Y, Mousavi T, Aramini M, Danaie M, Grovenor C R M and Speller S C 2022 Understanding irradiation damage in high-temperature superconductors for fusion reactors using high resolution x-ray absorption spectroscopy *Commun. Mater.* **3** 8

[18] Sickafus K E, Willis J O, Kung P J, Wilson W B, Parkin D M, Maley M P, Clinard F W, Salgado C J, Dye R P and Hubbard K M 1992 Neutron-radiation-induced flux pinning in Gd-doped $YBa_2Cu_3O_{7-x}$ and $GDBA_2Cu_3O_{7-x}$ *Phys. Rev.* B **46** 11862–70

[19] Gray R L, Rushton M J D and Murphy S T 2022 Molecular dynamics simulations of radiation damage in $YBa_2Cu_3O_{7-x}$ *Supercond. Sci. Technol.* **35** 035010

[20] Weber H W 2011 Radiation effects on superconducting fusion magnet components *Int. J. Mod. Phys.* E **20** 1325–78

[21] Emhofer J, Eisterer M and Weber H W 2013 Stress dependence of the critical currents in neutron irradiated (RE)BCO coated conductors *Supercond. Sci. Technol.* **26** 035009

[22] Nordlund K *et al* 2018 Primary radiation damage: a review of current understanding and models *J. Nucl. Mater.* **512** 450–79

[23] Weber H W, Böck H, Unfried E and Greenwood L R 1986 Neutron dosimetry and damage calculations for the TRIGA MARK-II reactor in Vienna *J. Nucl. Mater.* **137** 236–40

[24] Devitre A R, Fischer D X, Woller K B, Clark B C, Short M P, Whyte D G and Hartwig Z S 2024 A facility for cryogenic ion irradiation and *in situ* characterization of rare-earth barium copper oxide superconducting tapes *Rev. Sci. Instrum.* **95** 063907

[25] Emhofer J 2012 Analysis of coupled coated conductors for fusion magnet applications *PhD Thesis* TU Wien https://repositum.tuwien.at/bitstream/20.500.12708/8778/2/Emhofer%20Johann%20-%202012%20-%20Analysis%20of%20coupled%20coated%20conductors%20for%20fusion%20magnet...pdf

[26] Xiong X, Kim S, Zdun K, Sambandam S, Rar A, Lenseth K P and Selvamanickam V 2009 Progress in high throughput processing of long-length, high quality and low cost IBAD MgO buffer tapes at superpower *IEEE Trans. Appl. Supercond.* **19** 3319–22

[27] Lao M, Hecher J, Sieger M, Pahlke P, Bauer M, Hühne R and Eisterer M 2016 Planar current anisotropy and field dependence of j_c in coated conductors assessed by scanning hall probe microscopy *Supercond. Sci. Technol.* **30** 024004

[28] Bean C P 1964 Magnetization of high-field superconductors *Rev. Mod. Phys.* **36** 31–39

[29] Nordlund K 1995 Molecular dynamics simulation of ion ranges in the 1–100 keV energy range *Comput. Mater. Sci.* **3** 448–56

[30] Grande P L and Schiwietz G 1994 Improved calculations of the electronic and nuclear energy losses for light ions penetrating H and He targets at intermediate velocities *Braz. J. Phys.* **24** 551–65 (available at: http://hdl.h andle.net/10183/118162)

[31] Thompson A P *et al* 2022 LAMMPS - a flexible simulation tool for particle-based materials modeling at the atomic, meso and continuum scales *Comput. Phys. Commun.* **271** 108171

[32] Stukowski A 2010 Visualization and analysis of atomistic simulation data with OVITO-the Open Visualization Tool *Modelling Simul. Mater. Sci. Eng.* **18** 015012

[33] Kresse G and Hafner J 1993 *Ab initio* molecular dynamics for liquid metals *Phys. Rev.* B **47** 558–61

[34] Kresse G and Furthmüller J 1996 Efficiency of *ab-initio* total energy calculations for metals and semiconductors using a plane-wave basis set *Comput. Mater. Sci.* **6** 15–50

[35] Kresse G and Furthmüller J 1996 Efficient iterative schemes for *ab initio* total-energy calculations using a plane-wave basis set *Phys. Rev.* B **54** 11169–86

[36] Blöchl P E 1994 Projector augmented-wave method *Phys. Rev.* B **50** 17953–79

[37] Kresse G and Joubert D 1999 From ultrasoft pseudopotentials to the projector augmented-wave method *Phys. Rev.* B **59** 1758–75

[38] Perdew J P, Burke K and Ernzerhof M 1996 Generalized gradient approximation made simple *Phys. Rev. Lett.* **77** 3865–8

[39] Monkhorst H J and Pack J D 1976 Special points for Brillouin-zone integrations *Phys. Rev.* B **13** 5188–92

[40] Ogunjimi V, Ann Sebastian M, Zhang Di, Gautam B, Jian J, Huang J, Zhang Y, Haugan T, Wang H and Wu J 2021 Enhancing magnetic pinning by $BaZrO_3$ nanorods forming coherent interface by strain-directed Ca-doping in $YBa_2Cu_3O_{7-x}$ nanocomposite films *Supercond. Sci. Technol.* **34** 104002

[41] Balatsky A V, Vekhter I and Zhu J-X 2006 Impurity-induced states in conventional and unconventional superconductors *Rev. Mod. Phys.* **78** 373–433

[42] Tolpygo S K, Lin J-Y, Gurvitch M, Hou S Y and Phillips J M 1996 Effect of oxygen defects on transport properties and t_c of $YBa_2Cu_3O_{6+x}$: displacement energy for plane and chain oxygen and implications for irradiation-induced resistivity and t_c suppression *Phys. Rev.* B **53** 12462–74

[43] Maeno Y, Tomita T, Kyogoku M, Awaji S, Aoki Y, Hoshino K, Minami A and Fujita T 1987 Substitution for copper in a high-t_c superconductor $YBa_2Cu_3O_7 - \delta$ *Nature* **328** 512–4

[44] Mendels P, Alloul H, Collin G, Blanchard N, Marucco J F and Bobroff J 1994 Macroscopic magnetic properties of Ni and Zn substituted $YBa_2Cu_3O\chi$ *Physica* C **235–240** 1595–6

[45] Kinoshita K, Kitano H, Maeda A, Nishizaki T, Maeda M, Shibata K and Kobayashi N 2004 Impurity effect on the electronic state of the vortex core in the mixed state of $YBa_2Cu_3O_y$ *Physica* C **412–414** 530–4